Journal of the Mechanics and Physics of Solids 59 (2011) 237–250

Contents lists available at ScienceDirect

Journal of the Mechanics and Physics of Solids

journal homepage: www.elsevier.com/locate/jmps

Multiscale modeling and characterization of granular matter: From grain kinematics to continuum mechanics

J.E. Andrade [a,*], C.F. Avila [a], S.A. Hall [b], N. Lenoir [c], G. Viggiani [b]

[a] Applied Mechanics, California Institute of Technology, Pasadena, CA 91125, USA
[b] Laboratoire 3S-R, Université Joseph Fourier, 38041 Grenoble Cedex 9, France
[c] Material Imaging, UR Navier, 77420 Champs-sur-Marne, France

ARTICLE INFO

Article history:
Received 2 March 2010
Received in revised form
7 October 2010
Accepted 30 October 2010
Available online 4 November 2010

Keywords:
Micro-structures
Constitutive behavior
Granular material
Multiscale
X-ray computed tomography

ABSTRACT

Granular sands are characterized and modeled here by explicitly exploiting the discrete-continuum duality of granular matter. Grain-scale kinematics, obtained by shearing a sample under triaxial compression, are coupled with a recently proposed multiscale computational framework to model the behavior of the material without resorting to phenomenological evolution (hardening) laws. By doing this, complex material behavior is captured by extracting the evolution of key properties directly from the grain-scale mechanics and injecting it into a continuum description (e.g., elastoplasticity). The effectiveness of the method is showcased by two examples: one linking discrete element computations with finite elements and another example linking a triaxial compression experiment using computed tomography and digital image correlation with finite element computation. In both cases, dilatancy and friction are used as the fundamental plastic variables and are obtained directly from the grain kinematics. In the case of the result linked to the experiment, the onset and evolution of a persistent shear band is modeled, showing—for the first time—three-dimensional multiscale results in the post-bifurcation regime with real materials and good quantitative agreement with experiments.

1. Introduction

Granular materials are defined as those composed of smaller particles, and in our case, those whose mechanical behavior is governed by the interaction between particles. Within this description, we embrace the discontinuum–continuum nature of granular materials (Muir Wood, 2004). At the grain scale, the material is clearly discontinuum and is mostly governed by Newtonian mechanics (for large enough particles). On the other hand, at a larger scale (e.g., meter scale), the material can be collectively described as a continuum, using standard continuum mechanics arguments. The seemingly disparate nature of the discontinuum–continuum duality in granular matter has fostered the development of models that rely on either discrete or continuum philosophies and has hence contributed to a gap in our knowledge of the material.

So far, the backbone of our models has been furnished by numerical techniques such as the finite element method (FEM) (Belytschko et al., 2000; Hughes, 1987) and the discrete element method (DEM) (Cundall and Strack, 1979). The FEM models have relied on continuum mechanics techniques that ultimately invoke phenomenological constitutive models (Desai and Siriwardane, 1984). These phenomenological models have occupied an important place in geomechanics due to their

* Corresponding author.
E-mail address: jandrade@caltech.edu (J.E. Andrade).

0022-5096/$ - see front matter © 2010 Elsevier Ltd. All rights reserved.
doi:10.1016/j.jmps.2010.10.009

versatility and ability to capture many of the most salient features in geomaterials such as soils, rocks and concrete (Andrade and Borja, 2006; Bažant et al., 2000; Dafalias and Popov, 1975; DiMaggio and Sandler, 1971; Grueschow and Rudnicki, 2005; Vermeer and de Borst, 1984). However, current models face limitations when dealing with applications outside the phenomenological realm: how can a phenomenological model accommodate changes in the micro-structure due to thermo-chemo-hydro-mechanical coupling during radioactive disposal or changes in the constitutive response once a landslide is triggered? Even basic features, such as deformation bands, governing the failure of geosystems, pose significant challenges for the constitutive description of the material inside the band (Desrues et al., 1996; Oda et al., 2004; Rechenmacher, 2006; Santamarina, 2001).

To understand and predict the behavior of granular materials at the continuum scale, one must recognize that their mechanical behavior is encoded at the grain scale. The discrete element method (DEM) was introduced to explicitly account for the grain as the fundamental block in these materials (Bardet and Proubet, 1991; Ng, 2009; Rothenburg and Bathurst, 1989). Unfortunately, DEM models suffer from two major shortcomings: high computational cost and, related to this, inability to capture grain shape accurately. Enlargement of particles and use of smooth particles such as spheres and ellipsoids renders the model as just another phenomenological method, where parameters—albeit physically intuitive—are tuned to capture the desired behavior (Tu and Andrade, 2008). Particle angularity and relevant scales cannot be accurately modeled by classical discrete methods at this point. However, it is clear that DEM is able to access the fundamental scale of granular materials and, as it becomes more accurate and computational power continues to increase, it will allow for faithful representation of granular materials from their most basic granular scale. Consequently, it is clear that a multi-scale approach combining the strengths of the FEM and DEM methods, while capturing the main features of the material, has yet to emerge.

Multiscale methods have emerged lately in mechanics to bridge different material scales ranging from atomic scale to continuum scale. These methods aim at obtaining constitutive responses at the continuum scale, without resorting to phenomenology. The pioneering quasi-continuum method proposed the use of the so-called Cauchy–Born rule to obtain a continuum energy density function from molecular dynamics computations within a finite region of interest (Tadmor et al., 1996). Another similar multiscale method is the recently proposed virtual power domain decomposition (Liu and McVeigh, 2008), which has been used to do concurrent and hierarchical simulations in solids with heterogeneities at multiple scales. Very recently, a FE^2 algorithm was proposed by Belytschko et al. (2008) to aggregate discontinuities across scales in highly distorted areas in solids. Even though the method has only been used within a continuum formulation so far, it promises to link particulate or molecular dynamics with continuum mechanics. Unfortunately, none of the aforementioned methods has focused on granular materials within a multiscale framework.

In the area of geomechanics, multiscale methods are beginning to emerge. Some efforts are being made to obtain more realistic models based on a multiscale philosophy, see, for example, Dascalu and Cambou (2008) and Wellmann et al. (2007). At this point, techniques linking the granular and continuum scales are dependent on homogenization theory (Nitka et al., 2009; Wellmann et al., 2007). Recently, a new multicale technique has been proposed to update plastic internal variables in continuum plasticity models based on micro-mechanical calculations at a unit cell, without resorting to phenomenological hardening laws or classic homogenization (Andrade and Tu, 2009; Tu et al., 2009). However, there are still fundamental questions that need to be addressed to better understand and model the mechanics and physics of granular matter across scales.

This paper presents a multiscale method that will help answer two fundamental questions in the context of granular materials such as sands:

1. What is the fundamental set of information to be passed between scales in a discrete-continuum material?
2. What is the role of micro-structure in the determination of material behavior at the continuum level?

The first question is pertinent to all multiscale methods and is vital to faithfully capture micro-mechanical behavior. The second question pertains to accurate modeling of real materials, since in the case of real sands and other geologic materials, grain shape plays a central role in influencing macroscopic mechanical response (Santamarina, 2001). We propose a hierarchical scheme with the objective of answering the aforementioned questions. The technique is coupled to computations and experiments to extract key micro-mechanical information. In particular, we extract the frictional resistance and dilatancy, which are known to be key variables in the macroscopic description of granular materials (Muir Wood, 1990; Reynolds, 1885). The coupling with computations helps us show that these two parameters are sufficient to describe the macroscopic behavior of the underlying granular model (hence answer the first question above). In a way this is a verification process, rather than validation in the sense that predictions by the multiscale process are only as accurate as the underlying discrete model.

To furnish a validation process, we use advanced experimental data obtained at the European Synchrotron Radiation Facility (ESRF). These rich experimental data, allow us to characterize the grain kinematics of real sands while sheared under axisymmetric compression (Hall et al., 2010). From these data, we also extract dilatancy and friction (using a stress-dilatancy relation) evolutions amenable to multiscale analysis. A persistent shear band appearing in the experiment is modeled accurately by invoking the multiscale technique within a finite element framework. Clearly, current micro-mechanical models are incapable of capturing the complex behavior of real granular materials such as sands. Nevertheless, the multiscale model is able to leverage the rich data obtained from the experiments and capture the kinematics and macroscopic response

implied by the persistent shear band in three dimensions for the first time. This example sheds light into answering the second question above and opens the door to developing more powerful models that rely on physics rather than phenomenology for granular matter.

The paper is organized in three parts: Introduction, multiscale framework, and representative multiscale computations. The multiscale framework describes the classic continuum elastoplastic model for granular matter, depicting clearly the role of the plastic internal variables friction and dilatancy. Also, the micro-mechanical description is furnished in this section by the discrete element method and grain kinematics obtained from experimental data using X-ray computed tomography and digital image correlation. Coupling approaches are introduced at the end of this section. Representative multiscale computations using both discrete element method and experimental data are shown next. Finally, the paper is concluded based on the presented model and the results obtained.

As for notations and symbols used in this paper, bold-faced letters denote tensors and vectors; the symbol ' $\cdot$ ' denotes an inner product of two vectors (e.g., $\boldsymbol{a}\cdot\boldsymbol{b}=a_ib_i$) or a single contraction of adjacent indices of two tensors (e.g., $\boldsymbol{c}\cdot\boldsymbol{d}=c_{ij}d_{jk}$); the symbol ':' denotes an inner product of two second-order tensors (e.g., $\boldsymbol{c}:\boldsymbol{d}=c_{ij}d_{ij}$) or a double contraction of adjacent indices of tensors of rank two and higher (e.g., $\boldsymbol{C}:\boldsymbol{\varepsilon}^{\mathrm{e}}=C_{ijkl}\varepsilon^{\mathrm{e}}_{kl}$); the symbol ' $\otimes$ ' denotes a juxtaposition, e.g., $(\boldsymbol{a}\otimes\boldsymbol{b})_{ij}=a_ib_j$. Finally, for any symmetric second order tensors $\boldsymbol{\alpha}$ and $\boldsymbol{\beta}$, $(\boldsymbol{\alpha}\otimes\boldsymbol{\beta})_{ijkl}=\alpha_{ij}\beta_{kl}$, $(\boldsymbol{\alpha}\oplus\boldsymbol{\beta})_{ijkl}=\alpha_{ik}\beta_{jl}$, and $(\boldsymbol{\alpha}\ominus\boldsymbol{\beta})_{ijkl}=\alpha_{il}\beta_{jk}$.

2. Multiscale framework

2.1. Continuum description: elastoplasticity

Consider the classical two-invariant linear elastic–plastic Drucker-Prager model. The elastic portion of the material behavior is given by the isotropic elastic tangent

$$\boldsymbol{c}^{\mathrm{e}}=K\boldsymbol{\delta}\otimes\boldsymbol{\delta}+2G\left(\boldsymbol{I}-\frac{1}{3}\boldsymbol{\delta}\otimes\boldsymbol{\delta}\right) \tag{2.1}$$

where K and G are the elastic bulk and shear moduli, and $\boldsymbol{I}$ and $\boldsymbol{\delta}$ are the fourth- and second-order identity tensors. As usual, the stress increment is related to the elastic strain increment via the generalized Hooke's law, i.e., $\dot{\boldsymbol{\sigma}}=\boldsymbol{c}^{\mathrm{e}}:\dot{\boldsymbol{\varepsilon}}^{\mathrm{e}}$. Also, the strain rate is split into elastic and plastic components by the additive decomposition assumption

$$\dot{\boldsymbol{\varepsilon}}=\dot{\boldsymbol{\varepsilon}}^{\mathrm{e}}+\dot{\boldsymbol{\varepsilon}}^{\mathrm{p}} \tag{2.2}$$

The inelastic response is encapsulated in the yield surface and plastic potential given by the first two invariants of the stress tensor, namely,

$$p=\frac{1}{3}\mathrm{tr}\,\boldsymbol{\sigma}\quad\text{and}\quad q=\sqrt{\frac{3}{2}}\|\mathrm{dev}\,\boldsymbol{\sigma}\| \tag{2.3}$$

with $\mathrm{tr}\square=\square:\boldsymbol{\delta}$ and $\mathrm{dev}\square=\square-1/3(\mathrm{tr}\square)\boldsymbol{\delta}$ as the trace and deviatoric operators for a second-order tensor, respectively, and $\|\square\|=\sqrt{\square:\square}$ as the L_2-norm for a second-order tensor. Usually, p is referred to as the mean stress and q as the deviatoric stress, thus describing independent invariants of the stress tensor. Similarly, one can define the first two invariants for the strain rate tensor $\dot{\boldsymbol{\varepsilon}}$ so that

$$\dot{\varepsilon}_{\mathrm{v}}=\mathrm{tr}\,\dot{\boldsymbol{\varepsilon}}\quad\text{and}\quad\dot{\varepsilon}_{\mathrm{s}}=\sqrt{\frac{2}{3}}\|\mathrm{dev}\,\dot{\boldsymbol{\varepsilon}}\| \tag{2.4}$$

Using the aforementioned invariants of the stress tensor, the yield surface and plastic potential for a Drucker–Prager-type nonassociative model for cohesionless materials can be postulated, i.e.,

$$F(p,q,\mu)=q+\mu p=0 \tag{2.5}$$

$$Q(p,q,\beta)=q+\beta p-\overline{c} \tag{2.6}$$

with μ typically referred to as the generalized friction coefficient, β is the plastic dilatancy, and $\overline{c}$ is a free parameter so that the plastic potential crosses the yield surface at the same stress state (p,q). Fig. 1 shows a schematic of the yield surface and plastic potential and the geometric meaning for the plastic internal variables (PIVs): μ, β, and $\overline{c}$. Finally, the nonassociative flow rule is given in the classic form with the direction of the plastic strain rate determined by the normal to the plastic potential so that

$$\dot{\boldsymbol{\varepsilon}}^{\mathrm{p}}=\dot{\lambda}\boldsymbol{q} \tag{2.7}$$

with $\boldsymbol{q}:=\partial Q/\partial\boldsymbol{\sigma}$. The scalar $\dot{\lambda}$ is called the consistency parameter and controls the magnitude of plastic strain rate. Using the definitions for the strain rate invariants and the particular form for $\boldsymbol{q}$ emanating from the Drucker–Prager model, one can obtain that

$$\dot{\varepsilon}^{\mathrm{p}}_{\mathrm{v}}=\dot{\lambda}\beta,\quad\dot{\varepsilon}^{\mathrm{p}}_{\mathrm{s}}=\dot{\lambda},\quad\beta=\frac{\dot{\varepsilon}^{\mathrm{p}}_{\mathrm{v}}}{\dot{\varepsilon}^{\mathrm{p}}_{\mathrm{s}}} \tag{2.8}$$

where it is clear that the plastic dilatancy β controls the volumetric plastic strain rate for a given deviatoric strain rate.

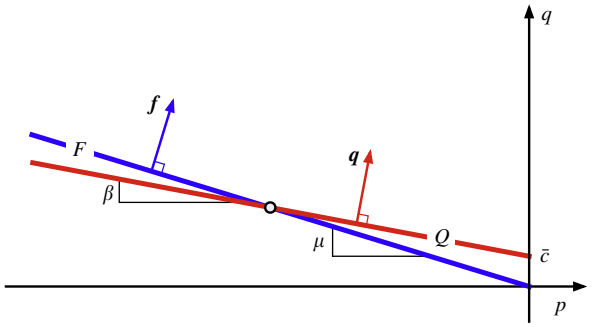

Fig. 1. Geometric attributes for Drucker–Prager-like model.

Table 1
Parameters used in classic DEM simulations and the values adopted in this study.

Symbol	Parameter	Value
k_n	Normal contact stiffness	1.0
k_t	Tangential contact stiffness	1.0
μ_p	Interparticle friction coefficient	0.5
c_n	Normal damping coefficient	0.05
c_t	Tangential damping coefficient	0.05

The canonical elastic perfectly plastic continuum tangent—relating the change in total strain to the change in stress—is then obtained by the generalized Hooke's law, the nonassociative flow rule, and the consistency condition at flow ($\dot{F}=0$), so that

$$\boldsymbol{c}^{ep}=\boldsymbol{c}^{e}-\frac{1}{\chi}\boldsymbol{c}^{e}:\boldsymbol{q}\otimes\boldsymbol{f}:\boldsymbol{c}^{e},\quad \chi:=\boldsymbol{q}:\boldsymbol{c}^{e}:\boldsymbol{f} \tag{2.9}$$

In the special case of the Drucker–Prager-type plasticity model considered herein, the gradient to the yield surface, $\boldsymbol{f}:=\partial F/\partial\boldsymbol{\sigma}$, and the gradient to the plastic potential $\boldsymbol{q}$ take the special form

$$\boldsymbol{f}=\frac{1}{3}\mu\boldsymbol{\delta}+\sqrt{\frac{3}{2}}\hat{\boldsymbol{n}} \tag{2.10}$$

$$\boldsymbol{q}=\frac{1}{3}\beta\boldsymbol{\delta}+\sqrt{\frac{3}{2}}\hat{\boldsymbol{n}} \tag{2.11}$$

where $\hat{\boldsymbol{n}}:=\operatorname{dev}\boldsymbol{\sigma}/\|\operatorname{dev}\boldsymbol{\sigma}\|$ is a unit tensor coaxial with the deviatoric component of the stress tensor.

Remark 1. The elastoplastic tangent in Eq. (2.9) is identical to that of a perfectly plastic model. The reason for this is that the PIVs in this multiscale plasticity model are *frozen* within loading increments (Andrade and Tu, 2009). However, the PIVs are allowed to update between loading increments. The evolution of the PIVs is obtained from the micro-structure, rather than a hardening law, and can be considered piecewise constant.

The plastic internal variables (PIVs) in this model are the frictional resistance μ and the plastic dilatancy β. Typically, the value of the PIVs have to be prescribed *a priori* or their evolution is tied to some kind of phenomenological hardening law. However, in this paper, we propose the evaluation of the PIVs directly from the micro-structure, using multiscale analysis. The micro-structural information will be provided either by discrete element method (DEM) calculations (e.g., Section 3.1) or detailed experiments (e.g., Section 3.2). In Section 2.3 we outline the procedure to link the elastoplastic framework presented in this section and the discrete mechanics described in the following section.

2.2. Discrete description: grain-scale kinematics

2.2.1. Discrete element method

The discrete element method (DEM) is used herein as a prototypical model to access grain-scale phenomena. DEM was developed by Cundall and Strack (1979) to explicitly account for the discrete nature of granular materials and, in principle, relies solely on the satisfaction of basic Newtonian mechanics. However, classic DEM models particles as rigid spheres, relying on linear contact stiffness (normal and tangential) and Coulomb friction for inelastic relative sliding in the tangential direction (Tu and Andrade, 2008). A list of typical material parameters used in DEM to govern interaction between particles is given in Table 1. As shown by Tu and Andrade (2008), proper calibration of these parameters is not trivial when modeling

quasi-static problems, as Newtonian mechanics imply dynamic processes and inertia effects and damping coefficients tend to lose physical meaning when applied to quasi-static situations.

Used with care, DEM can enable us to examine the grain-scale mechanisms governing the macroscopic behavior of granular media under quasi-static and dynamic conditions. In this study, we perform quasi-static simulations using DEM under axisymmetric or 'triaxial' conditions. Fig. 2 shows the topology of the numerical sample, composed of 1800 poly-disperse spheres, and the loading conditions. The numerical model is very similar to that used in a previous study by Tu et al. (2009). From the micro-mechanical simulations, it is of interest to calculate the average stress $\overline{\boldsymbol{\sigma}}$ and average strain tensor $\overline{\boldsymbol{\varepsilon}}$. Within a unit cell of volume V the average micro-mechanical stress is obtained by invoking standard equilibrium conditions (Christoffersen et al., 1981), i.e.,

$$\overline{\boldsymbol{\sigma}} = \mathrm{sym}\left[\frac{1}{V}\sum_{n=1}^{N_c} \boldsymbol{l}^n \otimes \boldsymbol{d}^n\right] \tag{2.12}$$

where $\boldsymbol{l}^n$ represents the contact force at contact point n, $\boldsymbol{d}^n$ denotes the distance vector connecting the two particles in contact at n, and N_c is the total number of contact points in the volume V of the unit cell.

Similar to the average micro-mechanical stress, the average micro-mechanical strain tensor $\overline{\boldsymbol{\varepsilon}}$ can be computed from the granular kinematics, specifically using the displacement field. However, the calculation of $\overline{\boldsymbol{\varepsilon}}$ is significantly more involved as it requires integration of the displacement field over the boundary of the unit cell. Following Wellmann et al. (2007), we introduce a discrete procedure exploiting the convex hull calculation proposed by Barber et al. (1996) to calculate surface areas using a triangular discretization so that

$$\overline{\boldsymbol{\varepsilon}} = \mathrm{sym}\left[\frac{1}{V}\sum_{n=1}^{N_t} \boldsymbol{u}^n \otimes \boldsymbol{v}^n A^n\right] \tag{2.13}$$

Fig. 3 shows a schematic of the triangular discretization and a close up into the main ingredients involved in the calculation. In the resulting procedure, the displacement $\boldsymbol{u}^n = 1/3(\boldsymbol{u}^{i,n} + \boldsymbol{u}^{j,n} + \boldsymbol{u}^{k,n})$ is the average of the displacements $\boldsymbol{u}^{i,n}$, $\boldsymbol{u}^{j,n}$, and $\boldsymbol{u}^{k,n}$ associated with particles i, j and k, which define the n-th triangle. The vector $\boldsymbol{v}^n$ defines the normal and A^n is the area of the n-th triangle. The dyadic products are summed over all the N_t triangles discretizing the surface area of the unit volume of measure V.

Using the average stress and strain measures introduced above, we can extract the current state of the particle assembly and use this information to perform multiscale computations by, for instance, extracting the PIVs introduced in the previous section. The multiscale procedures used to perform this extraction will be discussed in Section 2.3.

Remark 2. Any other model to simulate the grain-scale is amenable with the proposed methodology. The procedure we propose relies solely on the ability to calculate the average micro-mechanical stress $\overline{\boldsymbol{\sigma}}$ and the average micro-mechanical strain $\overline{\boldsymbol{\varepsilon}}$. Ideally, these average measures of the state should capture the real behavior of granular materials. In the case of spherical DEM, this is not possible if we are trying to extract the micro-structural behavior of angular materials, such as sands. However, the purpose of the method shown here is to extract the micro-mechanical behavior encapsulated in the grain-scale model, which in this case is given by DEM. Other, perhaps more accurate models, can be used as well. The ultimate multiscale model is as accurate as the underlying micro-mechanical model.

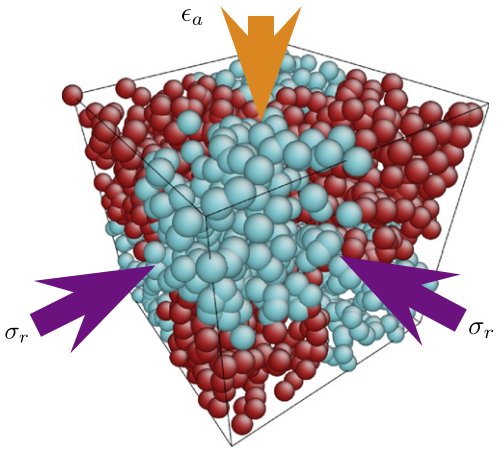

Fig. 2. Initial configuration and loading conditions for DEM model composed of 1800 poly-disperse spheres. Different colors represent domain decomposition into eight sub-domains corresponding to the different octants of the cubical specimen. (For interpretation of the references to color in this figure legend, the reader is referred to the web version of this article.)

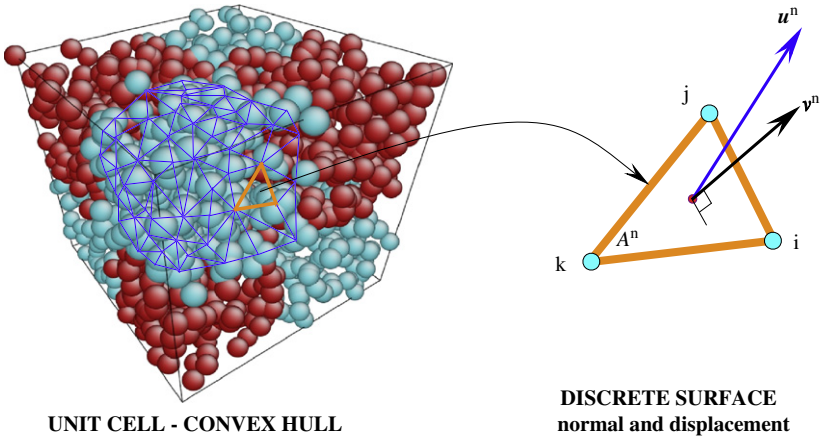

Fig. 3. Unit cell surface discretized using triangular elements defined by the centroids of particles associated with the boundary. Inset shows the n-th triangle and its associated nodes, average displacement $\boldsymbol{u}^n$, normal $\boldsymbol{v}^n$, and surface area A^n.

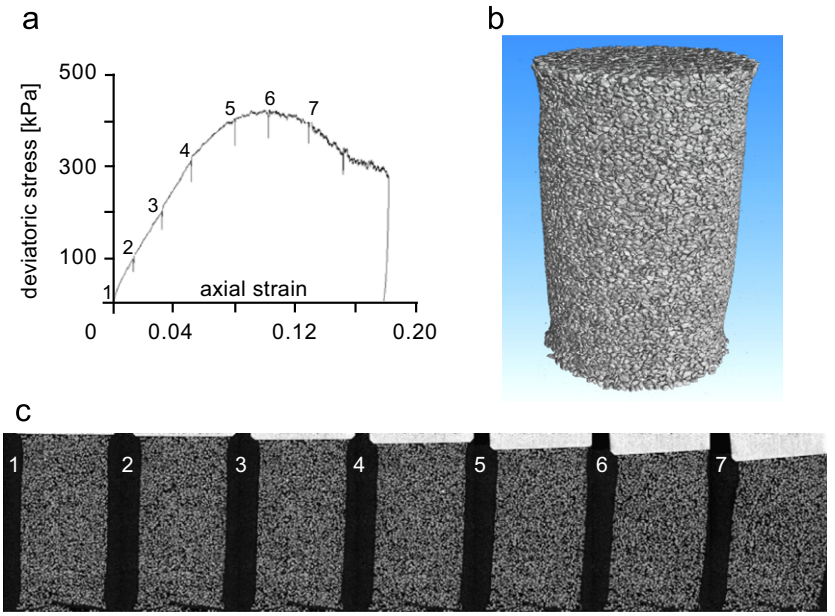

Fig. 4. Data from X-ray CT during triaxial compression of sand sample with spatial resolution of 14 μm, mean grain diameter of 300 μm and dimensions of 11 by 22 mm. (a) Global stress–strain curve, (b) initial micro-structure, (c) slices showing changes in micro-structure at points shown in stress–strain curve (top gray feature appearing after stage 2 is loading platen and shows tilting at stage 7). Adapted from Hall et al. (2010).

2.2.2. *In situ computed tomography and three-dimensional digital image correlation*

An initially dense sample of angular sand was sheared under axisymmetric, i.e., 'triaxial' compression, at the European Synchrotron Radiation Facility (ESRF). In addition to three-dimensional tomographic images, three-dimensional image correlation (3D-DIC) techniques were used to extract local information about the displacement field in the sample while deformation was in progress. Detailed reports of this experimental study are presented elsewhere (Hall et al., 2010). Some of the main results are presented here for completeness.

Fig. 4 shows some of the main results from this novel experimental study. A cylindrical sample of Hostun sand with 11 mm in diameter and 22 mm in height was sheared in a specially designed triaxial apparatus (Lenoir, 2006; Lenoir et al., 2007). The global deviator stress, as a function of the axial strain, is reported in Fig. 4(a). The curve shows a clear peak followed by a pronounced softening response. Fig. 4(b) shows the initial configuration of the sample, and part (c) of the figure shows several cross-sections corresponding to the stages marked on part (a) where tomographic images of the sample were taken.

The tomographic images were captured using $14 \times 14 \times 14\,\text{micron}^3$ μm resolution voxels to characterize particles with mean grain diameter around 300 μm. A constant cell pressure of 100 kPa was used along with a constant deformation rate of 60 μm/min in the axial direction. These loading conditions are analogous to those used in the DEM sample shown in Fig. 2. DIC

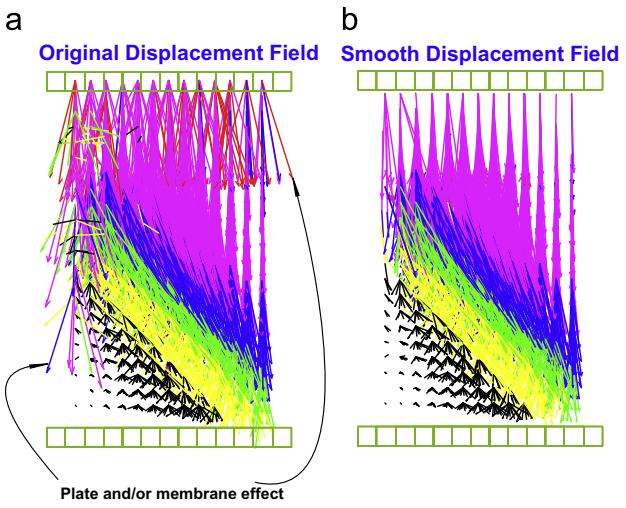

Fig. 5. Incremental displacements from DIC enhanced X-ray tomography between stages 6 and 7 in Fig. 4(a) (post-peak response). Raw incremental displacements are shown in (a) whereas (b) shows incremental displacements after cells adjacent to the platens and membrane are removed. The figure shows a clear persistent shear band near the center of the specimen. Green cells represent top and bottom platens. (For interpretation of the references to color in this figure legend, the reader is referred to the web version of this article.)

was used in concert with tomographic images to compute local values of the three-dimensional displacement field. Fig. 5 shows the incremental displacement field between tomographic stages 6 and 7 (post-peak in the load–displacement curve). Part (a) of the figure shows the incremental displacement vectors obtained by DIC using cells containing 27 particles on average. Some large incremental displacements are observed, likely a product of the boundary effects stemming from the DIC technique itself and the sample membrane. For modeling purposes, the boundary cells were cropped out in this study, yielding 'smooth' incremental displacement vectors such as those shown in Fig. 5(b). These incremental displacements (between stages) and the global stress–strain curve shown in Fig. 4(a), will be used in Section 3.2 to perform hierarchical multiscale computations and predict the global stress–strain curve as well as the evolution of a persistent shear band observed in the sub-granular scale resolution experiments.

2.3. *Linking elastoplasticity and grain-scale kinematics*

Following the procedure proposed by Andrade and Tu (2009), we exploit the physical significance of the plastic internal variables (PIVs) to extract them directly from the micro-structural state represented by $\overline{\boldsymbol{\sigma}}$ and $\overline{\boldsymbol{\varepsilon}}$. In the case of the friction coefficient, it can be calculated using the invariants of the average stress tensor $\overline{\boldsymbol{\sigma}}$, calculated directly from the grain structure (see Eq. (2.12)). Compatibility with the yield condition $F=0$ (see Eq. (2.5)) implies:

$$\mu \approx -\frac{\overline{q}}{\overline{p}} \tag{2.14}$$

with $\overline{p}$ and $\overline{q}$ as the invariants of the average stress tensor $\overline{\boldsymbol{\sigma}}$.

Similarly, plastic dilatancy (or dilatancy in short), can be extracted by making the approximation that plastic strain rates dominate so that $\dot{\boldsymbol{\varepsilon}} \approx \dot{\boldsymbol{\varepsilon}}^{\mathrm{p}}$, and therefore,

$$\beta \approx \frac{\Delta\overline{\varepsilon}_{\mathrm{v}}}{\Delta\overline{\varepsilon}_{\mathrm{s}}} \tag{2.15}$$

In the above equation, the strain rates are approximated using finite differences, where $\Delta\square := \square_{n+1} - \square_n$ and represents the change in $\square$ at time stage t_{n+1} relative to that at time stage t_n. The incremental strain $\Delta\overline{\boldsymbol{\varepsilon}}$ is calculated first and then its invariants $\Delta\overline{\varepsilon}_{\mathrm{v}}$ and $\Delta\overline{\varepsilon}_{\mathrm{s}}$ are computed based on the definition for the strain invariants given in Eq. (2.4). In the case of DEM-based calculations, the average strain $\overline{\boldsymbol{\varepsilon}}$ is calculated at every time stage for each unit cell using Eq. (2.13). On the other hand, in the case of the experiment-based computations the incremental strain $\Delta\overline{\boldsymbol{\varepsilon}}$ is calculated using Eq. (3.1), based on the finite element interpolations and the incremental displacement data obtained from DIC.

Fig. 6 shows the essence of the hierarchical multiscale calculation procedure used in this study. A sequential hierarchical scheme is chosen in this study to facilitate numerical implementation, however, the multiscale technique is amenable to concurrent or semi-concurrent implementations as shown by Andrade and Tu (2009) and Tu et al. (2009). Here, we follow the taxonomy provided by Mei (2009), where a hierarchical multiscale method is labeled as one where the two scales are not coupled directly, but rather provide data that can be used hierarchically as the calculations are coarsened or upscaled. In this case, the DEM or experimental data are used to extract the complete evolution of PIVs by using the procedures outlined above. Hence, as in Fig. 6, the PIVs evolution is extracted for every unit cell in the DEM or experimental tests and then used

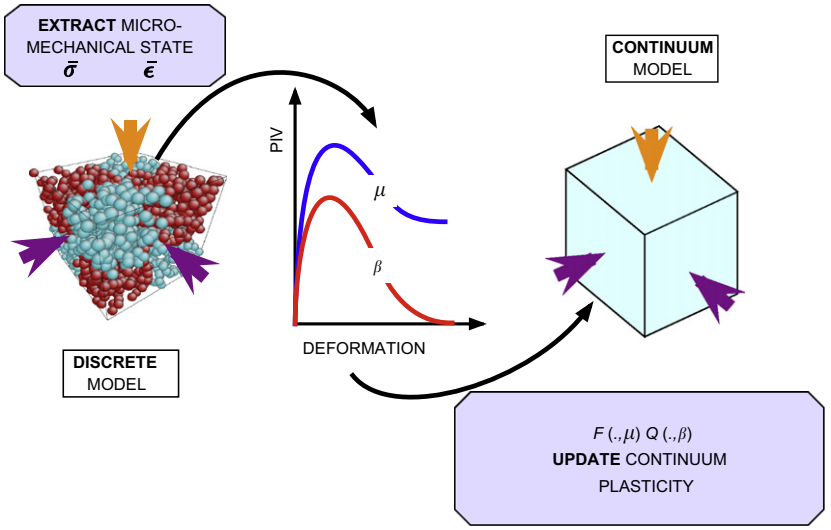

Fig. 6. Schematic showing hierarchical multiscale calculation to extract micro-mechanical state (stress and strain) and use it to obtain the evolution of the plastic internal variables (PIVs) as a function of the deformation. These PIVs are subsequently used to update the plasticity model used in continuum calculations. The discrete model could be either DEM or experiments.

hierarchically to provide an evolution of the PIVs in the finite element continuum formulation. In this way, the PIVs are extracted from the micro-scale directly, using boundary conditions consistent with the macro-scale (FEM) calculations, therefore bypassing phenomenological evolution laws for the PIVs. Specific examples of this technique are provided in the next section to show the validity of the method against the backdrop of both numerical DEM simulations (e.g., Section 3.1) and experiment-based calculations (e.g., Section 3.2).

Remark 3. It should be noted that in the case of DEM calculations, both μ and β can be extracted directly from the micro-structure. However, in the case of experiments, the average stress tensor $\overline{\boldsymbol{\sigma}}$ is not readily available and hence, only dilatancy β can be directly calculated from the change in the average strain tensor. Therefore, a so-called stress–dilatancy law needs to be invoked so that (Muir Wood, 1990)

$$\mu = \beta + \mu_{cv} \tag{2.16}$$

So, once a value of β is obtained, μ can be obtained using the above equation. The parameter μ_{cv} is usually called the residual frictional resistance at critical state or when $\beta = 0$ and is typically treated as a material constant, at least under quasi-static loading. The concept of stress–dilatancy is well established in the plasticity of granular matter literature.

3. Representative multiscale simulations

3.1. DEM-based multiscale computations

The assembly shown in Fig. 2 was used to perform both direct numerical simulations and hierarchical multiscale computations. As mentioned before, the total assembly contained 1800 polydisperse particles and was divided into eight unit cells—shown in different colors—to demonstrate the ability of the scheme to perform calculations using multiple cells and its potential for parallelization.

The boundary conditions imposed on the granular assembly are axisymmetric or 'triaxial'. Initially, the assembly is consolidated isotropically to a confining pressure of 170 kPa. After the isotropic consolidation, the radial stresses σ_r are kept constant (at 170 kPa) and the axial strain ε_a is increased incrementally as to compress the sample, as show in Fig. 2. The shearing phase was achieved by imposing a compressive axial strain rate of $2E-4\,s^{-1}$ for a total of 2.5 s. The micro-mechanically based stress $\overline{\boldsymbol{\sigma}}$ and strain $\overline{\boldsymbol{\varepsilon}}$ were calculated using Eqs. (2.12) and (2.13), respectively, for each of the eight unit cells in the granular sample, at each time increment in the calculation. The stress and strain invariants were then used in Eqs. (2.14) and (2.15) to extract the friction and dilatancy evolution curves as a function of deviatoric strain shown in Fig. 7. Each unit cell was used to extract its own evolution of friction μ and dilatancy β. Additionally, the global stress and strain response obtained from the DEM simulation were also used to compute a global average stemming from the direct numerical simulation (termed DEM global in Fig. 7).

The evolution of the plastic internal variables, obtained for each unit cell during the axisymmetric compression loading program using DEM, is then used hierarchically according to Fig. 6. The evolution curves for μ and β are passed sequentially to eight corresponding trilinear 'brick' finite elements that are then used to predict the global response of a continuum sample subjected to the same 'triaxial' compression conditions described before. The global average mechanical response is

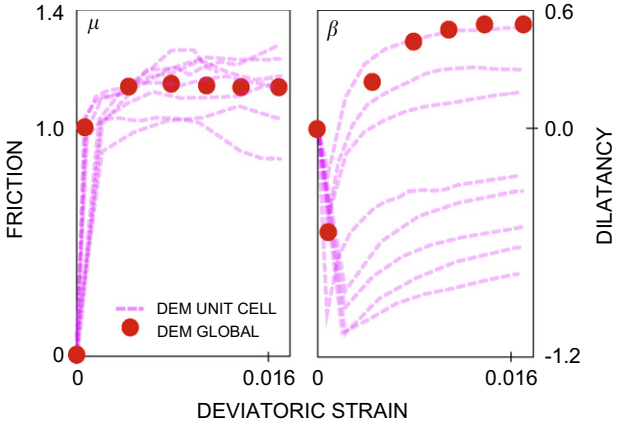

Fig. 7. Plastic internal variable evolution from DEM computations (direct numerical simulation). Friction and dilatancy are extracted for each unit cell (pink curves). Additionally, the global stress and strain are used to calculate the global evolution of the PIVs stemming from the entire sample in the direct numerical simulation (red points). It is observed that the unit cells furnish a distribution around the global PIV values. (For interpretation of the references to color in this figure legend, the reader is referred to the web version of this article.)

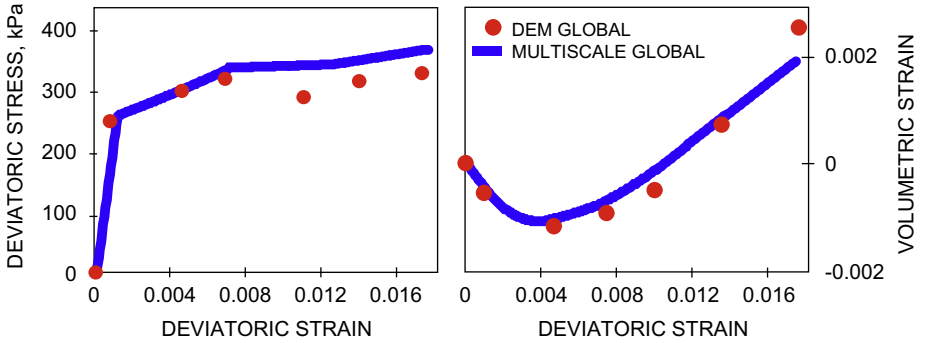

Fig. 8. Stress–strain response comparing DNS and multiscale calculations. The hierarchical simulations use the evolution of the PIVs obtained in Fig. 7 to predict the stress–strain response of the material using FEM. The multiscale calculation captures the essence of the mechanical response encapsulated in the discrete system modeled by DEM.

encapsulated in the calculation of the global deviatoric stress and global volumetric strain, plotted as a function of the global average deviatoric strain in Fig. 8. The average stress–strain responses calculated using the hierarchical multiscale technique are compared against those obtained from the DEM calculations. The global average responses are computed using a geometric average over all the integration points involved in the calculation (eight integration points per finite element). The elastic constants necessitated by the linear elastic model are naturally calibrated using the linear portion of the DEM stress–strain calculation (below 250 kPa). The two elastic constants are the only macroscopic parameters that need calibration in this framework.

These results show the ability of the proposed hierarchical multiscale technique to extract the mechanical behavior of granular materials under quasi-static conditions faithfully, without resorting to phenomenological evolution laws for the plastic internal variables (PIVs). The method has been used within semi-concurrent multiscale calculations for a singe unit cell in Andrade and Tu (2009) and Tu et al. (2009). However, these new results show the method is amenable to hierarchical calculations as well as multi-cell calculations. This is important for practical purposes where several 'hot' areas (e.g., inside shear bands) in an object need to be simulated using multiscale techniques 'on-the-fly'. Additionally, the results highlight that the multiscale method seems to capture fairly well the granular response elucidated by the underlying granular model (DEM in this case). Nevertheless, one open question is whether the method can capture real material response in complex granular materials such as sands. We attempt to answer this question in the next section using the data described in Section 2.2.2.

Remark 4. We have looked at the effect of using a larger unit cell, specifically, by taking the unit cell to be the whole granular assembly. Obviously, this yields more accurate results for homogeneous cases such as the one presented in this section (the response curves generated in Fig. 8 are even closer to their DEM counterpart). For the results presented above, it is clear from Fig. 7 that the behavior from each unit cell is different from the overall sample, nevertheless, the global behavior is well-reconstructed. In general, the issue of unit cell size is case-specific and is dominated by heterogeneity in the material

response. For example, Oda et al. (2004) showed clear evidence of the heterogeneity of void spaces inside shear bands. On the other hand, Tordesillas and Shi (2009) showed the importance of force chains in the behavior of granular matter, especially near and after failure. Unit cell sizes will have to be selected such that the key features of the material behavior are captured. In this paper, we do not focus on the rigorous selection of unit cell sizes *per se*. Rather, our discussion focuses on the information to be passed between scales such that these meso-scale effects are implied in the stress–strain relation at the macro-scale. More studies around the impact of unit cell sizes will be conducted in the near future.

3.2. Experiment-based multiscale computations

In this section, the localized incremental displacement fields and global stress–strain curve obtained experimentally and presented in Section 2.2.2 are used to perform hierarchical multiscale computations to predict the structural response of an analogous numerical sample. The idea is to link regions of the experimental sample, discretized by unit cells, with equivalent regions in a numerical sample, discretized with brick finite elements. As shown in Fig. 9, the nodes of a three-dimensional mesh using brick finite elements are defined by the centroids of the unit cells from the experiment. Doing so, allows us to associate the incremental displacements, obtained at the centroids of unit cells in the experiments, with a particular node in the finite element mesh. Then, finite element technology can be used to extract local information from the sample.

Fig. 10 shows the finite element mesh used to discretize the cylindrical sample and obtain a history of deformation as a function of the global loading program imposed. The figure also shows a progression or history of deviatoric deformations within each element. This is obtained using finite element interpolations (Fish and Belytschko, 2008), i.e.,

$$\Delta\boldsymbol{\varepsilon}^{\mathrm{e}} = \boldsymbol{B}^{\mathrm{e}}\Delta\boldsymbol{d}^{\mathrm{e}} \tag{3.1}$$

where $\Delta\boldsymbol{\varepsilon}^{\mathrm{e}}$ is the incremental strain over element e, $\Delta\boldsymbol{d}^{\mathrm{e}}$ is the incremental displacement vector containing the nodal incremental displacements (obtained experimentally), and $\boldsymbol{B}^{\mathrm{e}}$ is the classic strain–displacement matrix, congruent with Voigt notation. Incremental strains are calculated over each Gauss integration point (eight integration points are used for the trilinear brick elements) and then used to compute the average incremental strain over the element. The respective deviatoric and volumetric invariants are extracted from each incremental strain over each element. An accumulation of the deviatoric strains is plotted in Fig. 10, where we note a single shear band at the end of the experiment and where total shear strains reach values of 0.3 at some locations.

The multiscale model presented in Section 2.3 requires calibration of two elastic constants and the evolution of the PIVs μ and β from the micro-scale. The elastic constants can be obtained from the global load–displacement curve by making an assumption about the Poisson ratio of the material. Typical Poisson ratio ν for sands is around 0.3. Assuming this value, the shear modulus of the material can be obtained from the apparently linear portion of the deviatoric stress versus axial strain

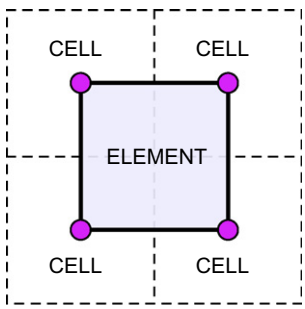

Fig. 9. Two-dimensional projection of unit cells and finite element mesh construction. Dashed lines describe unit cell regions in the experiment, whose centroids (circles) define the nodes used to construct finite elements. At these centroids/nodes, incremental displacements obtained in the experiment (cf., Fig. 5) are imposed and later interpolated to obtain incremental deformations as per Eq. (3.1).

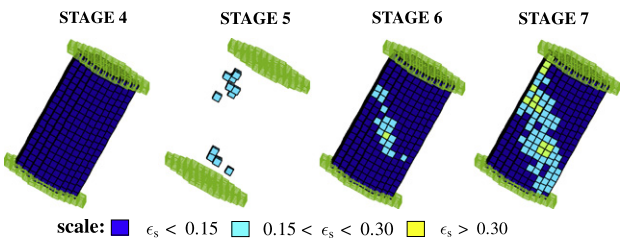

Fig. 10. Deviatoric strain history corresponding to the different stages as described in Section 2.2.2. The figure shows a progression of shear strain developing near the center of the specimen where a single persistent shear band is observed. In step between stages 4 and 5, only the elements undergoing high shear strains are shown for clarity and to illustrate the three-dimensional nature of the band.

curve shown in Fig. 4(a). We assume linear elastic behavior up to stage 4, around 0.05 axial strain. Note the sample is loaded under a constant radial stress of 100 kPa and there was no direct measure of radial strains. The estimated shear modulus of the material G comes up to be 2.6 MPa. Together, G and ν dictate the elastic behavior of the material, cf. Eq. (2.1).

Unlike in numerical simulations by DEM, the experimental results cannot be used to extract measurements of the stresses locally (at least not yet). As shown in Eq. (3.1), only local deformation fields can be reconstructed from the experimental data. Hence, only dilatancy β can be inferred from the experimental data. The frictional resistance μ is a function of the state of stress and will be inferred indirectly in this study. To approximate the value of dilatancy, we recur to a well-established concept in soil mechanics: a stress–dilatancy relationship (Muir Wood, 1990; Schofield and Wroth, 1968). A typical stress–dilatancy relation is given in Remark 3 in Eq. (2.16). We will use this stress–dilatancy relation and will hence need to calculate the value of frictional resistance at constant volume μ_{cv} during the critical state or when dilatancy is all spent ($\beta = 0$). We assume that the value of μ_{cv} is a material constant and it is hence the same for the entire specimen. Since we have assumed that the material is linear-elastic (and homogeneous) up to loading stage 4 (up to about 0.05 axial strain in the triaxial compression experiment), we further assume that plastic deformations follow after stage 4 and that dilatancy is nil at the beginning of the plastic process. Accordingly, the residual frictional strength at that point, according to the stress–dilatancy relation, would be $\mu = \mu_{cv} = -q/p$ and, therefore, the corresponding residual strength $\mu_{cv} \approx 300/200 = 1.5$ for the entire sample.

Remark 5. The assumption of elastic deformations up to stage 4 or about 0.05 axial strain is mostly based on the apparent linear portion observed in Fig. 4(a). Furthermore, this assumption facilitates greatly the modeling process. Also, it meshes well with the dilatancy (and plastic) process starting from zero, since the sample does compress during the elastic process, as expected from a relatively dense sample. Subsequent positive dilation will be responsible for the ensuing dilative process.

The central ingredient of the hierarchical multiscale model is the extraction of dilatancy β from each unit cell as a function of time, in order to obtain the complete evolution for the PIVs from the micro-structural process. This can be achieved using the aforementioned incremental strains stemming from the incremental displacements obtained using DIC linked to X-ray CT data (see Fig. 5 and Eq. (3.1)). Fig. 11(a) shows the values of dilatancy β calculated for every element in the sample during the incremental step between stages 6 and 7 (post-peak). From Fig. 10, it can be seen that a persistent shear band forms near the center of the sample. Deviatoric strains start accumulating between stages 4 and 5 (pre-peak) and continue to accumulate as loading progresses. As shown in Fig. 11(a), we model the average evolution of dilatancy by selecting the unit cells in the central portion of the sample and those unit cells that display average shear strains above 0.15. The central portion of the sample is used to extract average material responses with as little influence from boundary effects as possible. For example, Fig. 4(c) shows that there is some buckling on the sample at stage 7 and hence, local strain values (and dilatancy) might be affected near the top and bottom platens. Fig. 11(b) shows the resulting average dilatancy as a function of the global deviatoric strain for all unit cells inside the shear band and in the central region of the specimen. For instance, point 7 on the dilatancy curve shown in Fig. 11(b) is obtained by averaging the dilatancy values of those cells inside the shear band and in the central portion of the sample (red points in Fig. 11(a)).

Remark 6. Incremental displacements between loading stages 7 and 8 were not used for computing dilatancy values since, as can be observed in Fig. 4(c), the sample appears to buckle at or after stage 7 (see tilting of loading platen), hence potentially affecting dilatancy values. Rather, we assumed that the dilatancy values inside the shear band at stage 8 approaches critical state ($\beta = 0$). This assumption is consistent with the apparent value of deviatoric stress at that stage.

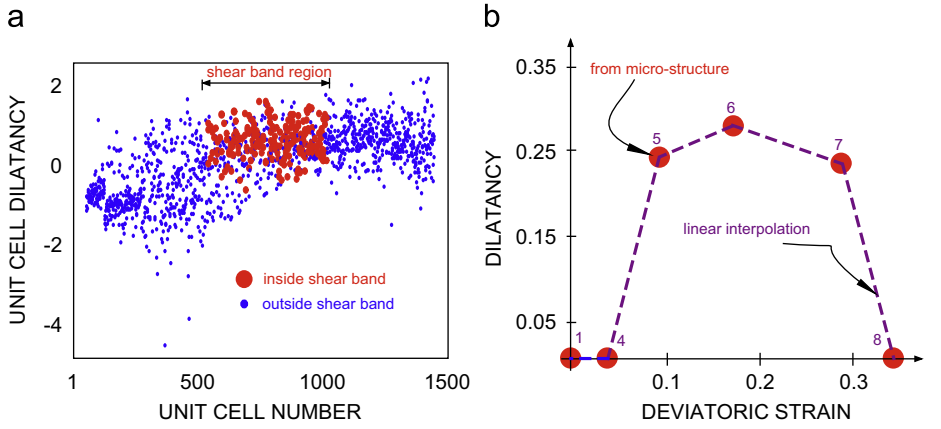

Fig. 11. (a) Dilatancy values for increment between deformation stages 6 and 7. Red dots represent values of dilatancy for elements inside the shear band and within the central portion of the sample. (b) Average dilatancy inside the shear band from incremental responses such as than shown in (b). Dilatancy is assumed to be nil during the elastic regime (from stage 1 to 4) and at stage 8 (critical state is assumed). (For interpretation of the references to color in this figure legend, the reader is referred to the web version of this article.)

Remark 7. As pointed out above, platen effects seem to appear around stage 6 in the loading program. These effects have been neglected in the current study for the sake of simplicity, as the objective of the paper is to establish an appropriate multiscale framework. However, more detailed studies about the effect of inhomogeneities, material and geometry will be conducted in the near future.

Once the average dilatancy β evolution is obtained for the elements inside the shear band, the structural response of the sample can be modeled using the hierarchical multiscale technique presented in this paper. As mentioned before, trilinear brick elements were used to model the cylindrical sample. The elastic material response is assumed to be homogenous and the evolution of the PIVs is assumed to be homogeneous (inside and outside the shear band) up to loading stage 6 (peak of the stress–strain curve). This is a modeling assumption, since the DIC with X-ray CT data shows inhomogeneous responses roughly after stage 4. This assumption simplifies the modeling effort significantly, and as we will show, does not affect the results significantly. After loading stage 6, the dilatancy evolution for the elements inside the shear band is governed by the curve in Fig. 11(b) and for those elements outside the shear band, it is assumed to stay at the peak value attained at stage 6 (around 0.3). This produces a state of inhomogeneous deformation after stage 6 (around 0.1 axial deformation), where the bulk of the deformation and the global response of the sample is governed by the evolution of the shear band.

Fig. 12 shows the global deviatoric stress versus the average nominal deviatoric strain of the sample computed from the hierarchical multiscale model and compared against the corresponding experimental global response. It can be seen that the stress–strain response of the numerical and physical samples agree very well. The multiscale model is able to capture the peak stress as well as the pronounced softening produced by the formation of the persisting shear band. Furthermore, the assumption of homogeneity up to the peak stress seems to be plausible, at least from a macroscopic standpoint. The deviatoric strains across the sample at loading stage 7 (about 0.13 axial strain), as calculated from the multiscale model and the experimental data, are reported in Fig. 13. It is evident that the multiscale model captures the magnitude of the shear strains as well as the overall topology of the persistent shear band.

The obtained results are quite encouraging for a variety of reasons. First, the hierarchical multiscale model is very simple, relying on a simple linear elastic response accompanied by a two-parameter plasticity model (friction and dilatancy). From these results, it seems plausible to suggest that μ and β do indeed capture the bulk of the material response, even in 'hot' areas such as shear bands. Second, these are, to the knowledge of the authors, the first multiscale results where direct comparison

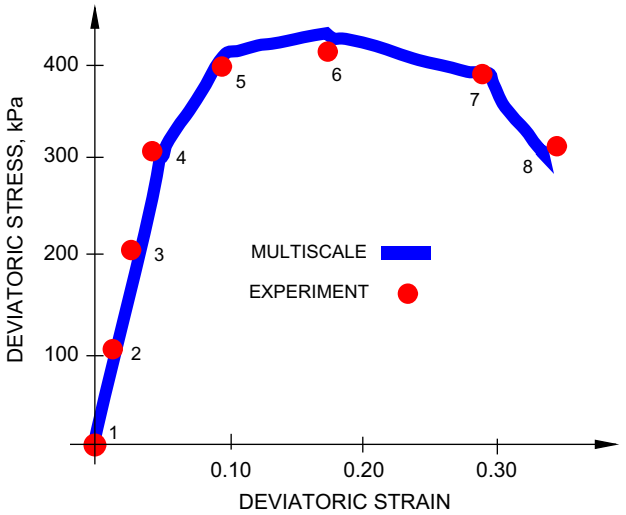

Fig. 12. Global average deviatoric stress versus global average deviatoric strain from hierarchical multiscale computation compared against the experimental response.

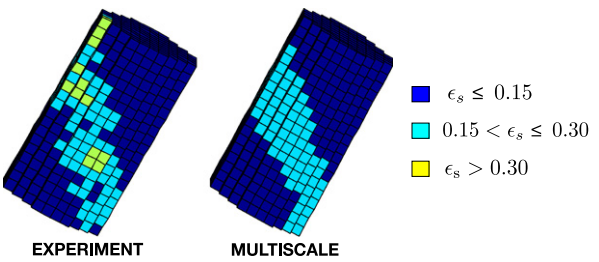

Fig. 13. Deviatoric strain map across the cylindrical sample at deformation stage 7 corresponding to a nominal axial strain around 0.13.

with experimental results have been made, at least for granular materials. This is not very surprising, since calculating the mechanical response of complex granular materials, such as sands, is not straightforward. Finally, these results are encouraging from the point of view of amalgamating advanced experimental results with multiscale computations to extract material behavior accurately. In the future, we will continue to use this approach to construct multiscale models that can predict the mechanical behavior from granular processes and then can be used to develop more powerful physics-based constitutive models.

4. Closure

In this paper, we have described a hierarchical multiscale procedure capable of reproducing the essential mechanical features of granular materials under shear loading. Both numerical and physical experiments were used to verify and validate the proposed method. The crux of the method is the extraction of two central plastic internal variables: friction and dilatancy. These are used in a simple elastoplastic model similar to a nonassociative Drucker–Prager. The multiscale technique extracts the plastic internal variables from the micro-structure directly and hence bypasses phenomenological evolution laws, typically invoked in modeling. Simulations based on underlying discrete mechanics (represented by the discrete element method) showed the potential of the procedure to extract information accurately from any discrete mechanics model. On the other hand, the computations based on advanced experimental data from DIC and X-ray CT, showed the ability of the model to extract real material behavior from complex three-dimensional micro-structures. In particular, a persisting shear band was observed in the experiment and accurately captured by the multiscale model. This is the first time that advanced experimentation and multiscale models are amalgamated, rendering more powerful and predictive multiscale models. These results may open the door to more physics-based constitutive models for complex engineering materials in the future.

Acknowledgments

We thank the anonymous reviewers for their insightful comments, which have improved the quality of this work. Support for this work was partially provided by NSF Grant no. CMMI-0726908, AFOSR Grant no. FA9550-08-1-1092, and DOE Grant no. DE-FG02-08ER15980. This support is gratefully acknowledged.

References

Andrade, J.E., Borja, R.I., 2006. Capturing strain localization in dense sands with random density. International Journal for Numerical Methods in Engineering 67, 1531–1564.
Andrade, J.E., Tu, X., 2009. Multiscale framework for behavior prediction in granular media. Mechanics of Materials 41, 652–669.
Barber, B., David, D., Hannu, H., 1996. The quick algorithm for convex hulls. ACM Transactions of Mathematical Software 22, 469–483.
Bardet, J.P., Proubet, J., 1991. Adaptive dynamic relaxation for statics of granular materials. Computers & Structures 39, 221–229.
Bažant, Z.P., Caner, F.C., Carol, I., Adley, M.D., Akers, S.A., 2000. Microplane model M4 for concrete. I: formulation with work-conjugate deviatoric stress. Journal of Engineering Mechanics 126, 944–953.
Belytschko, T., Liu, W.K., Moran, B., 2000. Nonlinear Finite Elements for Continua and Structures. John Wiley & Sons Ltd, West Sussex, UK.
Mei, X., 2009. Concurrent coupling of atomistic and continuum models. In: Multiscale Methods: Bridging the Scales in Science and Engineering. Oxford University Press.
Belytschko, T., Loehnert, S., Song, J.-H., 2008. Multiscale aggregating discontinuities: a method for circumventing loss of material stability. International Journal for Numerical Methods in Engineering 73, 869-894.
Christoffersen, J., Mehrabadi, M.M., Nemat-Nasser, S., 1981. A micromechanical description of granular material behavior. Journal of Applied Mechanics 48, 339–344.
Cundall, P.A., Strack, O.D.L., 1979. A discrete numerical model for granular assemblies. Géotechnique 29, 47–65.
Dafalias, Y.F., Popov, E.P., 1975. A model of nonlinearly hardening materials for complex loadings. Acta Mechanica 21, 173–192.
Dascalu, C., Cambou, B., 2008. Multiscale approaches to geomaterials. Acta Geotechnica 3.
Desai, C.S., Siriwardane, H.J., 1984. Constitutive Laws for Engineering Materials. Prentice-Hall, Inc.
Desrues, J., Chambon, R., Mokni, M., Mazerolle, F., 1996. Void ratio evolution inside shear bands in triaxial sand specimens studied by computed tomography. Géotechnique 46, 527–546.
DiMaggio, F.L., Sandler, I.S., 1971. Material model for granular soils. Journal of the Engineering Mechanics Division-ASCE 97, 935–950.
Fish, J., Belytschko, T., 2008. A First Course in Finite Elements. John Wiley & Sons Ltd., Chichester, West Sussex, UK.
Grueschow, E., Rudnicki, J.W., 2005. Elliptic yield cap constitutive modeling for high porosity sandstone. International Journal of Solids and Structures 42 (16–17), 4574–4587.
Hall, S.A., Bornert, M., Desrues, J., Pannier, Y., Lenoir, N., Viggiani, G., Bésuelle, P., 2010. Discrete and continuum analysis of localized deformation in sand using X-ray micro CT and volumetric digital image correlation. Géotechnique 60, 315–322.
Hughes, T.J.R., 1987. The Finite Element Method. Prentice-Hall, Englewood Cliffs, NJ.
Lenoir, N., 2006. Comportement mécanique et rupture das les roches argileuses étudiés par micro tomographie á rayons X. Ph.D. Thesis, Université Joseph Fourier, Grenoble, France.
Lenoir, N., Bornert, M., Desrues, J., Bésuelle, P., Viggiani, G., 2007. 3D digital image correlation applied to X-ray microtomography images from triaxial compression tests on argillaceous rock. Strain 43, 193–205.
Liu, W.K., McVeigh, C., 2008. Predictive multiscale theory for design of heterogeneous materials. Computational Mechanics 42, 147–170.
Muir Wood, D., 2004. Geotechnical Modelling. Spon Press, Taylor & Francis Group, London.
Muir Wood, D., 1990. Soil Behaviour and Critical State Soil Mechanics. Cambridge University Press, Cambridge, UK.
Ng, T.T., 2009. Shear strength and micro-descriptors of bidisperse ellipsoids under different loading paths. Mechanics of Materials 41, 748–763.
Nitka, M., Bilbie, B., Combe, G., Dascalu, C., Desrues, J., 2009. A micro–macro (DEM–FEM) model of the behavior of granular solids. In: 1st International Symposium on Computational Geomechanics (ComGeo I), Juan-les-Pins, France, pp. 38–48.
Oda, M., Takemura, T., Takahashi, M., 2004. Microstructure in shear band observed by microfocus X-ray computed tomography. Géotechnique 54, 539–542.

Rechenmacher, A.L., 2006. Grain-scale processes governing shear band initiation and evolution in sands. Journal of the Mechanics and Physics of Solids 54, 22–45.
Reynolds, O., 1885. On the dilatancy of media composed of rigid particles in contact. Philosophical Magazine and Journal of Science 20, 468–481.
Rothenburg, L., Bathurst, R.J., 1989. Analytical study of induced anisotropy in idealized granular materials. Géotechnique 39, 601–614.
Santamarina, J.C., 2001. Soils and Waves. John Wiley & Sons Ltd., New York.
Schofield, A., Wroth, P., 1968. Critical State Soil Mechanics. McGraw-Hill, New York.
Tadmor, E., Ortiz, M., Phillips, R., 1996. Quasicontinuum analysis of defects in solids. Philosophical Magazine A 73, 1529–1563.
Tordesillas, A., Shi, J., 2009. Micromechanical analysis of failure propagation in frictional materials. International Journal for Numerical and Analytical Methods in Geomechanics 33, 1737–1768.
Tu, X., Andrade, J.E., 2008. Criteria for static equilibrium in particulate mechanics computations. International Journal for Numerical Methods in Engineering 75, 1581–1606.
Tu, X., Andrade, J.E., Chen, Q., 2009. Return mapping for nonsmooth and multiscale elastoplasticity. Computer Methods in Applied Mechanics and Engineering 198, 2286–2296.
Vermeer, P.A., de Borst, R., 1984. Non-associated plasticity for soils, concrete and rock. Heron 29, 1–62.
Wellmann, C., Lillie, C., Wriggers, P., 2007. Homogenization of granular material modeled by a three-dimensional discrete element method. Computers and Geotechnics 35, 394–405.